Diffusion-induced stress amplification in phase-transition materials for electrodes of lithium-ion batteries

International Journal of Mechanical Sciences 281 (2024) 109541

Contents lists available at ScienceDirect

International Journal of Mechanical Sciences

journal homepage: www.elsevier.com/locate/ijmecsci

Diffusion-induced stress amplification in phase-transition materials for electrodes of lithium-ion batteries

Davide Clerici

Department of Mechanical and Aerospace Engineering, Politecnico di Torino, Corso Duca degli Abruzzi, 24, 10129, Torino, Piemonte, Italy

ARTICLE INFO

Keywords:
Lithium ion battery
Multi-physics model
Electrochemical–mechanical model
Diffusion induced stress
Concentration-dependent partial molar volume

ABSTRACT

This work sheds the light on the stress amplification in active material particles of electrodes caused by the localized lithium concentration inhomogeneity due to phase transitions. This is a significant issue usually neglected in the literature, as generally the ideal Fickian diffusion model is used to describe the lithium diffusion, which particularly fails when dealing with phase change materials, resulting in the underestimation of the stress. In turn, this results in the underestimation of the fracture behavior of the electrode and the battery degradation, ultimately.

To overcome these limitations, this work proposes a mechanical-transport model where the lithium transport is modeled according to the non-ideal solution theory with an equivalent diffusion coefficient depending on the potential of the host material vs Li/Li^+. The results show that the proposed model correctly describes the concentration distribution within the particle of phase-change materials (graphite is chosen as a case study), in agreement with the existent experimental measurements. The differences with respect to the traditional Fickian diffusion model is substantial as the stress is up to 85% higher with the proposed model and the concentration distribution can capture the inhomogeneity caused by phase transitions.

1. Introduction

Mechanical phenomena play a significant role in the degradation of lithium-ion batteries (LIBs), and they have been attracting increasing attention in the last years. Mechanics is strictly coupled to electrochemical phenomena in lithium ion batteries electrodes [1,2]: the electrode microstructure (i.e. the active material particles) deforms according to the quantity of lithium ions intercalated, impacting the macroscopic deformation of the battery, as demonstrated with experimental measurements in relevant works [3,4]. Furthermore, lithium ions are unevenly distributed in the active material particle because of their diffusion, leading to differential strain and stress ultimately [5–7]. Comprehensive reviews about modeling the stress in the electrode microstructure can be found in relevant papers [8,9].

Such stresses result in the mechanical degradation of the electrode microstructure because of fracture propagation, that was quantified by the author with finite element models [10–12] as well as with an analytical method [13,14]. Fracture mechanics in electrodes for LIBs has been reviewed in relevant papers from the experimental [15] and modeling [16] point of view. Crack propagation in electrodes triggers undesired electrochemical processes leading to battery degradation ultimately [17]. Then, the development of models which accurately estimate the stress in the electrode microstructure are meaningful to evaluate the electrode damage [18], and thus the battery degradation [19–21].

Lithium ions transport and stress in the active material particles have been modeled in several works in the literature since the early '00 [5,22,23], starting from the pioneer work of Christensen and Newman [24]. These models are based on the ideal solution model [25] and a Fickian diffusion approach, namely lithium ions are driven by their concentration gradient and by the hydrostatic stress gradient. Furthermore, they consider the coupling between mechanical and diffusion phenomena with a concentration-dependent diffusion coefficient, which takes into account the positive influence of mechanical stress on lithium ions' diffusion [26,27]. In 2020, the author found an analytical solution to this problem [26,28], and further studies evaluated the influence of the shape and the size of the particles on the stress [7,29].

Few more refined models consider the phase-change behavior of some active materials and its influence on the concentration distribution. To this end, mainly three thermodynamic approaches were followed: non-ideal solution theory, "shrinking core" model, and Cahn–Hilliard free energy functional.

The thermodynamics of lithium transport in different intercalation compounds is reviewed in [30], and deepened in [31] where the diffusion of lithium ions in the two-phase transition is considered. The thermodynamic approach describes the changes in the crystal structure (phase change) according to thermodynamic quantities, such as the

E-mail address: davide.clerici@polito.it.

https://doi.org/10.1016/j.ijmecsci.2024.109541
Received 14 March 2024; Received in revised form 26 June 2024; Accepted 1 July 2024
Available online 7 July 2024

Nomenclature

Symbols

$\bar{D}$	Concentration dependent diffusion coefficient
c or c_{LiS}	Lithium ion concentration in intercalated sites
C_{rate}	Current rate
k_m	Mechanical constant
N	Lithium ion flux
R_g	Gas constant
V_0^M	Molar volume of pure species
x_{LiS}	Mole fraction of intercalated lithium ions
df	Thermodynamic driving force
A	Surface
D	Diffusion coefficient
E	Young modulus
e	electron
F	Chemical strain function
F	Faraday constant
R	Particle radius
r	Radial coordinate
S	Host site
T	Temperature
t	Time
U	Equilibrium potential
u	Displacement
V	Volume

Acronyms

DIS	Diffusion induced stress
FEM	Finite element method
GITT	Galvanostatic Intermittent Titration Technique
LCO	Lithium cobalt oxide
LFP	Lithium iron phosphate
Li	Lithium ion
LIB	Lithium ion battery
P2D	Partial two dimension
SEM	Scanning electron microscope

Greek Symbols

α	Thermodynamic factor
γ	Activity coefficient
μ_i	Chemical potential of species i
ν	Poisson ratio
Ω	Partial molar value
ρ	Density
σ	Stress
ε_v	Volumetric strain

Recursive subscripts

+	Positive charge
−	Negative charge
0	initial
c	Circumferential
h	Hydrostatic
LiS	Intercaled site with lithium ions
max	maximum
mech	mechanical
min	minimum
r	Radial
S	Vacant site
sf	Strain free

Gibbs free energy and the chemical potential. The thermodynamic properties of the active material are got simply by tracking the electrode potential [30]. As a result, any chemical or structural change of the electrode material is detected by its potential.

Non-ideal solution theory introduces the thermodynamic factor to measure the deviation of the intercalation compound from thermodynamic ideality (ideal solution or Fickian diffusion), being equal to 1 in case of ideal solution. The thermodynamic factor is computed from the electrode potential with respect to a lithium metallic reference electrode, and significantly deviates from 1 when phase transitions occur, as will be explained in Section 2.2.1. Few works [32–35], starting from the model of Christensen and Newman [24], modeled the concentration distribution in phase-change materials with the non-ideal solution theory. In 2018, Baker and Verbrugge [36,37] developed the so called multi-species multi-reaction (MSMR) model, to account for the multiple current peaks observed in voltammetry data related to phase transitions. Indeed, Tavassol et al. [38] showed that transitions between phases of the host material are manifested as peaks in the current response during cyclic voltammetry; On the other hand, phase transitions are manifested as voltage plateaus or equivalently as peaks in the derivative of capacity with respect to voltage during galvanostatic cycling. Nevertheless, MSMR model does not attempt to quantify stress due to phase transitions, modeled just from the electrochemical point of view.

Another approach consists in deriving the chemical potential from the Cahn–Hilliard free energy functional [39], usually adopted in the cases where the material shows a marked two-phase diffusion behavior. In these cases, the Cahn–Hilliard free energy functional is implemented in a phase-field model and governs the time evolution of lithium concentration [40,41]. Phase field models are a powerful tool for modeling diffusion in these materials because they are particularly accurate in the regions with sharp concentration gradients and they can treat phase boundaries without the need to explicitly track interfaces, as it is done with the “shrinking core” models. Narrowing the field to electrode materials, the phase transition of lithium iron phosphate (LFP) has been modeled with this kind of approach, as the diffusion consists in the movement of the boundary between the lithium-rich and the lithium-poor phase [42,43].

Finally, the “shrinking core” or “sharp interface” model is a non-Fickian model which considers the equilibrium concentrations among two coexistent phases and explicitly computes the movement of the boundary between the two phases [44]. Different models calculated concentration and stress with the “shrinking core” model within LFP [45–47], lithium cobalt oxide (LCO) [44,48] and amorphous/crystalline silicon [49] electrodes. A general model was proposed as well [50].

A constant partial molar volume was considered in almost all the models in the literature as far as the authors know, although it is known that several materials, such as graphite [51–53] and nickel manganese cobalt (NMC) [54–56], have a concentration-dependent partial molar volume. Variable partial molar volume was considered just in the works aiming to compute battery deformation [57–59], and not the full transport-mechanical problem.

In this work, the author aims to rise the attention about the diffusion-induced stress amplification in the electrode particles because

of the phase change of the host material during lithium insertion, resulting in highly localized concentration inhomogeneity and thus stress amplifications. This fact is of great interest because most models quantifying stress in active material particles, used to study crack propagation and battery degradation, do not account for stress amplification due to phase transitions, potentially underestimating degradation. In this context, this work develops a transport-mechanical model based on the non-ideal solution diffusion model, allowing to capture the influence of the phase change of the host material in the lithium concentration distribution and the resulting amplification of the diffusion-induced stress. Furthermore, the work proposes a methodology to consider a concentration dependent partial molar volume from the results of XRD analysis. Partial molar volume is typically assumed constant, but this assumption may be incorrect for phase change materials, as different phases formed at varying lithium contents have distinct structural arrangements.

The model framework proposed in this work has the great advantage that allows to take into account a complex phenomenon like phase transitions without increasing the computation complexity. Indeed, the influence of phase transitions is considered by defining an equivalent diffusion coefficient $D = D_0(\alpha + kc)$, where the thermodynamic factor α depending on the potential of the host material vs Li/Li^+ takes into account the influence of phase transition on lithium diffusion. When phase transitions are not considered, α is set equal to 1, coming back to the traditional diffusion-mechanical models [26].

The model is applied to a graphite electrode and it is solved with the finite element approach implemented in Comsol Multiphysics. The resulting concentration distribution is compared with the experimental measurements in graphite electrode available in literature, showing that the proposed model accurately describes the concentration trend observed experimentally with different in-situ techniques [60–63]. Furthermore, the non linear deformation captured by the concentration dependent partial molar volume is verified with dilatometry experiments reported in the literature [51]. Finally, it is shown that the concentration inhomogeneity caused by phase transitions captured by the non-ideal solution model significantly affects the resulting stress, with stress amplification up to 85% with respect to the case obtained with the traditional ideal solution model proposed in the literature. This proves the meaningfulness of considering phase transitions when computing diffusion-induced stress in electrode's active material particles.

2. Methods

Lithium transport and mechanical phenomena are tightly coupled in the electrodes of LIBs [25,26,64]. In this section, both the models are deepened to compute the concentration distribution, strain, and stress during operation. The non-ideal solution theory with concentration-dependent partial molar volume is proposed, being the most general approach and suitable to deal with phase-change material. Furthermore, a couple of simplifications are proposed, making proper hypotheses suitable for some classes of materials.

The domain is assumed spherical, in agreement with the scanning electrode microscope (SEM) observations of active material particles [15]. The material is isotropic and linear elastic and the boundary conditions are axisymmetric. Then, all the equations are written just in the particle radial coordinate according to the axisymmetric hypothesis.

The isotropic assumption is reasonable because even if the particles of some kind of electrode materials are made of smaller secondary particles (such as NMC) or domains (such as graphite), these constituents are randomly oriented, resulting in an homogeneous behavior. The linear elastic hypothesis is realistic for the intercalation materials, on the other hand alloying materials such as silicon shows a plastic deformation because of the huge volume deformation. Nevertheless, the transport theory delineated herein is applicable to intercalation materials, which are by far the most common materials used in LIBs.

Furthermore, the diffusion of lithium ions is considered isotropic. This assumption is true for most of the electrode materials except for LFP, which has an anisotropic diffusion [42,43].

2.1. Mechanical equations

Traditionally, the mechanical strain of the host material is assumed linearly dependent on the concentration of the solute (lithium ions) according to Eq. (1)a [65]. This assumption is valid if the partial molar volume is constant. In general, electrode materials exhibit different lattice structures (known as phases) as a function of the concentration of lithium ions. Each phase has a different volume, and partial molar volume accordingly. This makes the partial molar volume dependent on the concentration of lithium ions, and the strain is not linear anymore. In this general case, the chemical strain is computed according to Eq. (1)b

$$\begin{cases} \varepsilon_{ch} = \dfrac{\Omega(c - c_{sf})}{3}; & \text{Constant } \Omega \quad \text{(a)} \\ \varepsilon_{ch} = \dfrac{1}{3}\int_{c_{sf}}^{c} \Omega \, dc; & \text{General concentration-dependent } \Omega \quad \text{(b)} \end{cases} \tag{1}$$

where ε_{ch} is the strain due to lithium concentration (c), Ω is partial molar volume and c_{sf} is the reference concentration in the "strain-free" condition.

Eq. (1)a–b are graphically represented in Fig. 1a–b, respectively.

The concentration-dependent partial molar volume of graphite is calculated from the experimental-measured volumetric strain [51] as expressed in Eq. (2) [54,57], and it is graphically reported for lithiation in Fig. 1b and numerically reported in Table C.3. A slight difference exists between the partial molar volume computed from lithiation and delithiation measurements.

$$\Omega = V_0^M \frac{\partial \varepsilon_v}{\partial n} \tag{2}$$

where V_0^M is the molar volume of pure graphite, n is the moles of lithium ions inserted in the lithiated graphite compound Li_xC_6 and ε_v is the volumetric strain of the graphite structure upon lithiation experimentally measured by Schweidler et al. [51]. In particular, they measured the crystallographic changes occurring in the graphite unit cell during lithiation with operando X-ray diffraction. Then, they computed volumetric strain from the changes in lattice parameters of the unit cell.

In this way, the partial molar volume is exact when there is a single phase, and it results linearly interpolated between two phases. Taking as example stage II ($Li_{0.5}C_6$) and stage I (LiC_6) of graphite, partial molar volume is exact when x=0.5 and x=1, and is linearly interpolated for intermediate values. Actually, there is no points in the material with concentration comprised between x=0.5 and x=1, except for the transient phase boundary between stage I and II. Then, the deformation is caused by the fraction of material with concentration x=0.5 (according to $\Omega(x = 0.5)$), plus the fraction of material with concentration x=1 (according to $\Omega(x = 1)$), in accordance with the rule of mixture.

The constitutive, congruence, and equilibrium equations reported in Eqs. (3)a–c govern the mechanical field in a spherical particle, further details can be found in a relevant author's previous work [26]. It is pointed out that the general constitutive equations ((3)a) are composed of the elastic term (first), and the chemical term (second), which depends on the concentration of intercalated lithium ions and links chemistry with mechanics. The chemical term can be expressed according to Eq. (1)a or (1)b in the case of constant or concentration-dependent partial molar volume, respectively.

$$\begin{cases} \varepsilon_r = \frac{1}{E}\left(\sigma_r - 2\nu\sigma_c\right) + \varepsilon_{ch}; \;\; \varepsilon_c = \frac{1}{E}\left[(1-\nu)\sigma_c - \nu\sigma_r\right] + \varepsilon_{ch}; & \text{Constitutive} \quad \text{(a)} \\ \varepsilon_r = \frac{\partial u}{\partial r}; \;\; \varepsilon_c = \frac{u}{r} & \text{Congruence} \quad \text{(b)} \\ \frac{\partial \sigma_r}{\partial r} + \frac{2}{r}(\sigma_r - \sigma_c) = 0 & \text{Equilibrium} \quad \text{(c)} \end{cases} \tag{3}$$

where σ_r, ε_r, σ_c, ε_c are radial and circumferential stress and strain, respectively, u is the radial displacement and ε_{ch} is the chemical strain.

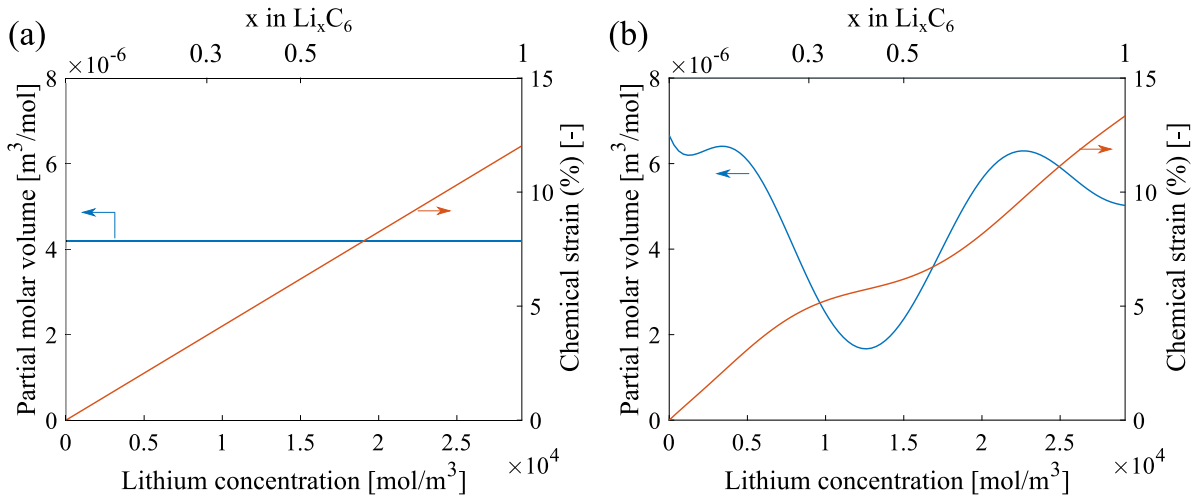

Fig. 1. Partial molar volume and chemical strain of graphite in case of (a) Constant partial molar volume and (b) Concentration-dependent partial molar volume. X-axis refers to the concentration of lithium ions in the host material.

The displacement solution is obtained writing the equilibrium Equation ((3)c) as a function of radial displacement (replacing the congruence and constitutive Equations ((3)a–b)), and integrating twice the resulting equilibrium equation with respect to the radial coordinate. Further details concerning this calculation are provided in Appendix A.

Two boundary conditions are applied: the radial stress is set to zero at the particle boundary ($r = R$), meaning that no mechanical interaction with other particles is considered, and the displacement is to zero at the particle center.

The radial displacement of each point in the particle is got in Eq. (4) after the application of the boundary conditions according to the computations reported in Appendix A.

$$u(r) = \frac{1+\nu}{1-\nu}\frac{3}{r^2}\int_0^r \varepsilon_{ch}(c(r))r^2\,dr + \frac{6(1-2\nu)}{1-\nu}\frac{r}{R^3}\int_0^R \varepsilon_{ch}(c(r))r^2\,dr \tag{4}$$

where ε_{ch} has expression reported in Eq. (1) according to the partial molar volume hypothesis. It is pointed out that the radial displacement in Eq. (4) comes back to the expression already known in literature [26] when a constant partial molar volume is considered (Eq. (1)a).

Radial and circumferential strains are computed with Eq. (3)b, replacing the displacement solution. The resulting expressions are reported in Eqs. (5).

$$\varepsilon_r(r) = \frac{(1+\nu)}{(1-\nu)}\left[\varepsilon_{ch}(c(r)) - \frac{2}{r^3}\int_0^r \varepsilon_{ch}(c(r))r^2\,dr\right] + \frac{2(1-2\nu)}{(1-\nu)}\frac{1}{R^3}\int_0^R \varepsilon_{ch}(c(r))r^2\,dr \tag{5a}$$

$$\varepsilon_c(r) = \frac{(1+\nu)}{(1-\nu)}\frac{1}{r^3}\int_0^r \varepsilon_{ch}(c(r))r^2\,dr + \frac{2(1-2\nu)}{(1-\nu)}\frac{1}{R^3}\int_0^R \varepsilon_{ch}(c(r))r^2\,dr \tag{5b}$$

The strain expressions come back to the expressions known in literature [26] if a constant partial molar volume is considered (Eq. (1)a).

Stresses are computed by rearranging the constitutive equations ((3)a) as reported in Eq. (6).

$$\sigma_r(r) = \frac{E\left[\left(\frac{\partial u}{\partial r} - \frac{1}{3}\int_{c_{sf}}^{c}\Omega\,dc\right)(1-\nu) + 2\nu\left(\frac{u}{r} - \frac{1}{3}\int_{csf}^{c}\Omega\,dc\right)\right]}{(1+\nu)(1-2\nu)} \tag{6a}$$

$$\sigma_c(r) = \frac{E\left[\left(\frac{u}{r} - \frac{1}{3}\int_{c_{sf}}^{c}\Omega\,dc\right)\nu + 2\nu\left(\frac{\partial u}{\partial r} - \frac{1}{3}\int_{csf}^{c}\Omega\,dc\right)\right]}{(1+\nu)(1-2\nu)} \tag{6b}$$

Then, the displacement solution reported in Eq. (4) is replaced in Eqs. (6) to get the stress solution (Eq. (7)a–b). Furthermore, hydrostatic stress (σ_h) is computed in Eq. (7)c.

$$\sigma_r(r) = \frac{2E}{(1-\nu)}\left[-\frac{1}{r^3}\int_0^r \varepsilon_{ch}(c(r))r^2\,dr + \frac{1}{R^3}\int_0^R \varepsilon_{ch}(c(r))r^2\,dr\right] \tag{7a}$$

$$\sigma_c(r) = \frac{E}{(1-\nu)}\left[\frac{1}{r^3}\int_0^r \varepsilon_{ch}(c(r))r^2\,dr + \frac{2}{R^3}\int_0^R \varepsilon_{ch}(c(r))r^2\,dr - \varepsilon_{ch}(c(r))\right] \tag{7b}$$

$$\sigma_h(r) = \sigma_r(r) + 2\sigma_c(r) = \frac{2}{9}\frac{E}{(1-\nu)}\left[\frac{9}{r^3}\int_0^R \varepsilon_{ch}(c(r))r^2\,dr - 3\varepsilon_{ch}(c(r))\right] \tag{7c}$$

The stress expressions come back to the expressions known in literature [26] if a constant partial molar volume is considered (Eq. (1)a).

It is emphasized that an analytical solution for displacement, strains, and stresses is obtained thanks to the spherical geometry, indeed a closed-form solution cannot be obtained in the more general case, even for the mechanical field.

At this stage, lithium concentration in intercalated sites (c) has to be computed with the transport problem, to explicitly determine the displacement, strain, and stress.

2.2. Transport equations

The concentrated or non-ideal solution model, explained in Section 2.2.1, is the most general approach to describe lithium transport and intercalation, resulting in a diffusion coefficient dependent on the concentration of lithium ions and the electrode potential vs Li/Li^+.

In Section 2.2.2, the ideal or dilute approach is considered: the diffusion coefficient is no longer dependent on the electrode potential, but the coupling between mechanical and transport equations is still considered.

Finally, the uncoupled model is considered in Section 2.2.3: the coupling between mechanical and transport equations is neglected, as well as the dependence of the diffusion coefficient on lithium concentration.

In each of the aforementioned models, the dependence of the partial molar volume on concentration can be either considered or neglected by adjusting the value of the chemical strain ε_{ch} in accordance with equation Eq. (1).

2.2.1. Non-ideal solution model

The binary solution theory considers li-intercalated sites (LiS) and vacant sites (S) in the host material, according to the reaction in Eq. (8).

$$Li^+_{electrolyte} + e^-_{matrix} + S_{host} \rightleftharpoons LiS_{host} \tag{8}$$

It can be referred to concentration of intercalated lithium ions (c_{LiS}) or their mole fraction (x_{LiS}) interchangeably, even if concentration is preferred in this work. The relation linking these two quantities is the following: $c_{LiS} = x_{LiS}c_{max}$, where c_{max} is the maximum concentration of lithium ions in the host material. For sake of brevity, c_{LiS} (concentration of intercalated sites) and c_S (concentration of vacant sites) are differentiated just in Section 2.2. Instead, c will be employed in place of c_{LiS} throughout the rest of this work to denote the lithium concentration in intercalated sites.

The thermodynamic potential driving the diffusion of lithium ions within the particle can be split into two contributions: chemical (μ_{LiS}) and mechanical (μ_{mech}), as expressed in Eq. (9)a. Constant temperature is assumed within the particle, then no thermal diffusion is considered.

The gradient of the thermodynamic potential drives lithium ions according to the thermodynamic driving force (df_{LiS}) expressed in Eq. (9)b [24].

$$\mu = \mu_{LiS} + \mu_{mech} = \left(\mu^0_{LiS} + R_gT\ln\left(\gamma_{LiS}\frac{c_{LiS}}{c_{max}}\right)\right) + (-\Omega\sigma_h) \tag{9a}$$

$$df_{LiS} = c_{LiS}\left(\nabla\mu_{LiS} - \Omega\nabla\sigma_h\right) \tag{9b}$$

where μ^0_{LiS} is the chemical potential at the reference state, T is the temperature, R_g is the gas constant and γ_{LiS} represents the activity correction taking into account the non-ideality of the solution. In the calculation of Eq. (9)b, the term $\nabla\Omega$ is neglected as it is a differential of greater order.

From Eq. (9) it results that lithium ions are driven from areas with higher concentration to areas with a lower concentration of lithium ions, and from areas in compression to tensile areas.

The molar flux (N_{LiS}) is defined in Eq. (10) according to Eq. (9) and assuming that the saturation concentration of lithium ions in the host (c_{max}) remains constant [32].

$$\begin{aligned} N_{LiS} &= -\frac{D}{R_gT}df_{LiS} \\ N_{LiS} &= -\frac{D}{R_gT}c_{LiS}\left[\nabla\mu_{LiS} - \Omega\nabla\sigma_h\right] = -\frac{D}{R_gT}c_{LiS}\left[\frac{\partial\mu_{LiS}}{\partial c_{LiS}} - \Omega\frac{\partial\sigma_h}{\partial c_{LiS}}\right]\nabla c_{LiS} \end{aligned} \tag{10}$$

where the diffusion coefficient of lithium in the host material is given by the term D.

The gradients of chemical potential and hydrostatic stress in Eq. (10) depend on lithium concentration, which depends on the radial coordinate in turn. Then, both the gradients are differentiated with respect to lithium concentration, and an explicit expression of $\frac{\partial\mu_{LiS}}{\partial c_{LiS}}$ and $\frac{\partial\sigma_h}{\partial c_{LiS}}$ is studied.

Starting considering the term $\frac{\partial\mu_{LiS}}{\partial c_{LiS}}$, the chemical potential of the specie LiS (μ_{LiS}) is reported in Eq. (11).

$$\mu_{LiS} = \mu^0_{LiS} + R_gT\ln(\gamma_{LiS}c_{LiS}) \tag{11}$$

Then, Eq. (12) reports the differential of the chemical potential of the specie LiS with respect to the lithium concentration c_{LiS}.

$$\begin{aligned} \frac{\partial\mu_{LiS}}{\partial c_{LiS}} = \frac{\partial}{\partial c_{LiS}}\left[R_gT ln(\gamma_{LiS}c_{LiS})\right] &= R_gT\frac{\partial}{\partial c_{LiS}}\left[ln(\gamma_{LiS}) + \ln(c_{LiS}) - ln(c_{max})\right] = \\ &= \frac{R_gT}{c_{LiS}}\left[\frac{\partial\ln(\gamma_{LiS})}{\partial\ln(c_{LiS})} + 1\right] = \\ &= \frac{R_gT}{c_{LiS}}\alpha \end{aligned} \tag{12}$$

$$\alpha = \left[\frac{\partial\ln(\gamma_{LiS})}{\partial\ln(c_{LiS})} + 1\right] \tag{13}$$

The parameter α in Eq. (13) considers the non-ideality of the solution and it is the so-called "thermodynamic factor". The expression in Eq. (13) cannot be quantified from experimental measurements. For this reason, the correlation between equilibrium potential and thermodynamic factor is investigated.

The equilibrium potential U of active material with respect to Li/Li^+ is expressed in Eq. (14).

$$FU = \mu^0_{Li} + \mu_S - \mu_{LiS} \tag{14}$$

where μ^0_{Li}, μ_S and μ_{LiS} are the chemical potential of pure lithium metal, vacant and li-intercalated sites in the host material, respectively and F is the Faraday constant.

Then, Eq. (14) is differentiated with respect to c_{LiS} resulting in Eq. (15).

$$F\frac{\partial U}{\partial c_{LiS}} = \frac{\partial\mu_S}{\partial c_{LiS}} - \frac{\partial\mu_{LiS}}{\partial c_{LiS}} \tag{15}$$

Furthermore, μ_S is isolated from the Gibbs–Duhem equation ($c_{LiS}d\mu_{LiS} + c_Sd\mu_S = 0$) and derived with respect to c_{LiS} in Eq. (16).

$$\frac{\partial\mu_S}{\partial c_{LiS}} = -\frac{\partial\mu_{LiS}}{\partial c_{LiS}}\frac{c_{LiS}}{c_S} \tag{16}$$

The differentiation term $\frac{\partial\mu_{LiS}}{\partial c_{LiS}}$ is got in Eq. (17) by replacing Eq. (16) in Eq. (15), and considering that the maximum concentration is the sum of the concentration of vacant and occupied sites ($c_{LiS} + c_S = c_{max}$).

$$\frac{\partial\mu_{LiS}}{\partial c_{LiS}} = -F(1 - \frac{c_{LiS}}{c_{max}})\frac{\partial U(c_{LiS})}{\partial c_{LiS}} \tag{17}$$

Finally, the thermodynamic factor is got in Eq. (18), equating Eq. (12) and Eq. (17).

$$\alpha(c_{LiS}) = 1 + \frac{\partial\ln(\gamma_{LiS})}{\partial\ln(c_{LiS})} = -\frac{F}{R_gT}c_{LiS}\left(1 - \frac{c_{LiS}}{c_{max}}\right)\frac{\partial U(c_{LiS})}{\partial c_{LiS}} \tag{18}$$

The thermodynamic factor can be estimated from potential measurements of the electrode material vs Li/Li^+ thanks to Eq. (18). The potential curve is flat where the two-phase reaction occurs, making the thermodynamic factor nearly zero, and eventually decreasing the chemical driving force (Eq. (12)), creating the concentration jump between the phases. The influence of the thermodynamic factor on diffusion during phase transitions will be better explained in Section 3.

The equilibrium potential and its derivative $\frac{\partial U}{\partial c_{LiS}}$ are functions of lithium concentration, then the thermodynamic factor makes the diffusion coefficient dependent on lithium content. The validity of the non-ideal theory is supported by Baker et al. [32], who showed that the diffusion coefficient measured with Galvanostatic Intermittent Titration Technique (GITT) fits pretty well with the composition-dependent diffusion coefficient computed with non-ideal theory. Similar results are also obtained by Latz et al. on LMO [66], showing that diffusion coefficient decreases when a phase transformation is occurring.

Now the term $\frac{\partial\sigma_{h,LiS}}{\partial c_{LiS}}$ in Eq. (10) is considered. The hydrostatic stress (Eq. (7)c) is derived with respect to the particle radius (r) in Eq. (19). The integral term in Eq. (7)c is constant with respect to the radius, then its derivative vanishes. The derivative of the chemical strain ε_{ch} with respect to the radius is equal to $\frac{\Omega}{3}\frac{\partial c}{\partial r}$, regardless of the assumption made on partial molar volume in Eq. (1): The case of constant partial molar volume (Eq. (1)a) is trivial. On the other hand, in the case of concentration-dependent partial molar volume (Eq. (1)b), the result is got considering the chain derivation rule ($\frac{1}{3}\frac{\partial}{\partial r}\int_{c_{sf}}^{c_{LiS}}\Omega dc_{LiS} = \frac{1}{3}\frac{\partial}{\partial c_{LiS}}(\int_{c_{sf}}^{c_{LiS}}\Omega dc_{LiS})\frac{\partial c_{LiS}}{\partial r}$).

$$\frac{\partial\sigma_h}{\partial r} = \frac{\partial\sigma_h}{\partial c_{LiS}}\frac{\partial c_{LiS}}{\partial r} = -\frac{2E\Omega}{9(1-\nu)}\frac{\partial c_{LiS}}{\partial r}\ ;\quad \frac{\partial\sigma_h}{\partial c_{LiS}} = -\frac{2E\Omega}{9(1-\nu)} \tag{19}$$

Eq. (19) is consistent with the results already found in literature in the case of constant partial molar volume [26].

The terms $\frac{\partial\mu_{LiS}}{\partial c_{LiS}}$ (Eq. (17)) and $\frac{\partial\sigma_h}{\partial c_{LiS}}$ (Eq. (19)) are replaced in the lithium molar flux (N_{LiS}) Eq. (10), resulting in Eq. (20)a.

$$N_{LiS} = -D\left[\alpha + k_mc_{LiS}\right]\frac{\partial c_{LiS}}{\partial r} = -\bar{D}(c_{LiS})\frac{\partial c_{LiS}}{\partial r} \tag{20a}$$

$$\bar{D}(c_{LiS}) = D\left[\alpha(c_{LiS}) + k_m(c_{LiS})c_{LiS}\right] \tag{20b}$$

$$k_m(c_{LiS}) = \frac{2E\Omega^2(c_{LiS})}{9(1-\nu)R_gT} \tag{20c}$$

Eq. (20)a is formulated as the Fick's law defining the concentration-dependent diffusion coefficient ($\bar{D}(c_{Lis})$) reported in Eq. (20)b. The dependence of the diffusion coefficient on the concentration of lithium is dual: (a) the term k_m models the coupling between transport and mechanical equations, as diffusion causes stress and stress affects diffusion reciprocally. (b) The thermodynamic factor α models the phase transitions of some active materials on the basis of their equilibrium potential vs Li/Li^+ (U), according to the non-ideal solution theory.

The mass of lithium ions is conserved within the particle according to Eq. (21), governing how the concentration of lithium ions changes in time within the particle as a result of the boundary molar flux (N_{LiS}). Eq. (21) is written in radial coordinates (r), taking advantage of the spherical symmetry of the particle.

$$\frac{\partial c_{LiS}}{\partial t} + \frac{1}{r^2}\frac{\partial}{\partial r}(r^2 N_{LiS}) = 0 \tag{21}$$

Finally, the lithium molar flux expressed in Eq. (20)a is replaced in the mass conservation law (Eq. (21)) to obtain the most general equation governing the transport of lithium ions within the active material particles (Eq. (22)). The boundary conditions consist of a time-dependent lithium flux $N_{surface}(t)$ over the particle boundary and zero flux at the particle center.

$$\begin{cases} \dfrac{\partial c_{LiS}}{\partial t} - D\left[(\alpha + k_m c_{LiS})\left(\dfrac{2}{r}\dfrac{\partial c_{LiS}}{\partial r} + \dfrac{\partial^2 c_{LiS}}{\partial r^2}\right) + \left(\dfrac{\partial \alpha}{\partial c_{LiS}} + \dfrac{\partial k_m}{\partial c_{LiS}}c_{LiS} + k_m\right)\left(\dfrac{\partial c_{LiS}}{\partial r}\right)^2\right] = 0 \\ \left.\dfrac{\partial c_{LiS}(r,t)}{\partial r}\right|_{r=R} = N_{surface}(t), \qquad \text{for t} \geq 0 \\ \left.\dfrac{\partial c_{LiS}(r,t)}{\partial r}\right|_{r=0} = 0, \qquad \text{for t} \geq 0 \end{cases} \tag{22}$$

where α and its derivative with respect to lithium concentration are reported in Eqs. (23)a–b, respectively.

$$\alpha = -\frac{F}{RT}c_{Lis}\left(1 - \frac{c_{Lis}}{c_{max}}\right)\frac{\partial U}{\partial c_{Lis}} \tag{23a}$$

$$\frac{\partial \alpha}{\partial c_{LiS}} = -\frac{F}{RT}\left[\left(1 - \frac{c_{Lis}}{c_{max}}\right)\frac{\partial U}{\partial c_{Lis}} - c_{LiS}\frac{\partial U}{\partial c_{Lis}} + c_{Lis}\left(1 - \frac{c_{Lis}}{c_{max}}\right)\frac{\partial^2 U}{\partial c_{LiS}^2}\right] \tag{23b}$$

The derivative of k_m in the case of concentration-dependent and constant partial molar volume (Ω) is reported in Eqs. (24)a and (24)b, respectively.

$$\frac{\partial k_m}{\partial c_{LiS}} = \frac{4E\Omega}{9(1-\nu)R_gT}\frac{\partial \Omega}{\partial c_{LiS}} \tag{24a}$$

$$\frac{\partial k_m}{\partial c_{LiS}} = 0 \tag{24b}$$

The problem in Eq. (22) cannot be computed analytically. Finite difference (FDM) [24,32,67] or finite element models (FEM) are usually employed, especially implemented in COMSOL Multiphysics [35,68].

2.2.2. Ideal solution model

This kind of model is used for modeling materials that do not have phase transitions. The interaction between lithium ions is not considered and the activity coefficient γ_{LiS} is equal to 1. Consequently, even α becomes equal to 1 according to Eq. (18), and the concentration-dependent diffusion coefficient ($\bar{D}(c_{LiS})$), reported in Eq. (20)b, changes according to Eq. (25)b.

$$N_{LiS} = -\bar{D}(c_{LiS})c_{max}\frac{\partial c_{LiS}}{\partial r} \tag{25a}$$

$$\bar{D}(c_{LiS}) = D[1 + k_m c_{LiS}] \tag{25b}$$

Then, the transport equation changes as reported in Eq. (26).

$$\begin{cases} \dfrac{\partial c_{LiS}}{\partial t} - D\left[(1 + k_m c_{LiS})\left(\dfrac{2}{r}\dfrac{\partial c_{LiS}}{\partial r} + \dfrac{\partial^2 c_{LiS}}{\partial r^2}\right) + \left(\dfrac{\partial k_m}{\partial c_{LiS}}c_{LiS} + k_m\right)\left(\dfrac{\partial c_{LiS}}{\partial r}\right)^2\right] = 0 \\ \left.\dfrac{\partial c_{LiS}(r,t)}{\partial r}\right|_{r=R} = N_{surface}(t) \qquad \text{for t} \geq 0 \\ \left.\dfrac{\partial c_{LiS}(r,t)}{\partial r}\right|_{r=0} = 0 \qquad \text{for t} \geq 0 \end{cases} \tag{26}$$

The analytical solution of the problem stated in Eq. (26) was found by the author in the case of constant partial molar volume exploiting the solution of the Fick's problem in Eq. (25), as detailed in the relevant publication [26].

The term k_m still considers the coupling between the transport and mechanical equations, and dependence of partial molar volume on lithium concentration can be either considered or neglected according to the expression of k_m and its derivative reported in Eq. (20)c and (24), respectively.

2.2.3. Uncoupled model

The uncoupled model neglects both the activity correction and the coupling between mechanical and transport equations, representing the simplest approach to the problem [26].

In this model, the mechanical potential is neglected, then the term $\Omega\nabla\sigma_h$ in the thermodynamic driving force (Eq. (9)b) vanishes, as well as the activity coefficient is considered equal to one, similarly to the model of Section 2.2.2. Then, the diffusion coefficient is no longer concentration-dependent and becomes equal to the nominal diffusion coefficient ($\bar{D} = D$). The lithium molar flux in Eq. (20) is rewritten according to Eq. (27).

$$N_{LiS} = -Dc_{max}\frac{\partial c_{LiS}}{\partial r} \tag{27}$$

Consequently, the transport equations for the uncoupled model are reported in Eq. (28).

$$\begin{cases} \dfrac{\partial c_{LiS}}{\partial t} - Dc_{max}\dfrac{\partial^2 c_{LiS}}{\partial r^2} = 0 \\ \left.\dfrac{\partial c_{LiS}(r,t)}{\partial r}\right|_{r=R} = N_{surface}(t) \quad \text{for t} \geq 0 \\ \left.\dfrac{\partial c_{LiS}(r,t)}{\partial r}\right|_{r=0} = 0 \qquad \text{for t} \geq 0 \end{cases} \tag{28}$$

Clearly, a concentration-dependent partial molar volume is meaningless in this model.

The stresses are overestimated in the uncoupled model because the coupling rises the diffusion coefficient, as the stress gradient is coherent with the concentration gradient and enhances the diffusion of lithium ions [26,28].

The possible expressions of the diffusion coefficient according to the model assumptions are reported in Table 1.

3. Results

The model is applied to a graphite electrode and it is implemented in Comsol Multiphysics. Further details about the model implementation and the customization of the built-in equations are reported in Appendix B. Graphite is particularly suitable to highlight the feature of the model explained in this work as it has a concentration-dependent partial molar volume, and it is characterized by three significant phase transitions in its lithiation window.

The operating current is defined as C-rate: 1C corresponds to the current required to completely fill the graphite particle in one hour. Then, the state of charge (SOC) is considered as the percentage of lithium ions filling the particle with respect to the maximum concentration and it is calculated as $SOC = c/c_{max}$. SOC is also equal to the moles

Table 1
Expressions of the diffusion coefficient and its terms according to the different model assumptions.

	Non-ideal solution	Ideal solution	
α	$-\frac{F}{RT}c_{Lis}\left(1-\frac{c_{Lis}}{c_{max}}\right)\frac{\partial U}{\partial c_{Lis}}$	1	
k_m	Concentration-dependent Ω $\frac{2E}{9(1-\nu)R_gT}\Omega^2(c_{LiS})$	Constant Ω $\frac{2E}{9(1-\nu)R_gT}\Omega^2$	Uncoupled 0
$\bar{D}$	Non-ideal solution Concentration-dependent Ω Coupled $D\left[\alpha+c_{LiS}k_m(c_{LiS})\right]$	Ideal solution Constant Ω Coupled $D\left[1+c_{LiS}k_m\right]$	Ideal solution – Uncoupled D

Table 2
Graphite material properties and operating conditions.

Property	Symbol	Value	u.m.	Ref.
Young modulus	E	15	GPa	[69,70]
Poisson ratio	ν	0.3	–	[24,69]
Density	ρ	2.10	$\frac{g}{cm^3}$	[24]
Molar volume	V_0^M	$34.96\,10^{-6}$	$\frac{m^3}{mol}$	[24]
Radius	R	10	μm	[71]
Zero strain concentration	c_{sf}	$0.01c_{max}$	$\frac{mol}{m^3}$	–
Maximum concentration	c_{max}	29 155	$\frac{mol}{m^3}$	Calculated
Initial concentration	c_0	Insertion: $0.01c_{max}$	$\frac{mol}{m^3}$	–
		Insertion : $0.97c_{max}$	$\frac{mol}{m^3}$	–
Constant partial molar volume	Ω	$4.2\,10^{-6}$	$\frac{m^3}{mol}$	Calculated
Diffusion coefficient	D	$2\,10^{-14}$	$\frac{m^2}{s}$	[72,73]
Operating conditions				
Temperature	T	298	K	–
Flux at 1C	N	$2.7\,10^{-5}$	$\frac{mol}{m^2 s}$	–

of lithium ions (x) in Li_xC_6. Depth of Discharge (DOD) is calculated as $DOD = 1 - SOC$.

The flux at the particle boundary is computed with Eq. (29), according to the C-rate.

$$N_{surface} = \frac{V c_{max} C_{rate}}{3600A} = \frac{R c_{max} C_{rate}}{3 \cdot 3600} \tag{29}$$

where A and V are the surface area and the volume of the particle.

Then, 1C corresponds to a lithium boundary flux equal to $2.7\,10^{-5}\,\frac{mol}{m^2 s}$, which multiplied by the Faraday constant gives a current density equal to $2.6\,A/m^2$, according to Eq. (29) using the graphite properties reported in Table 2.

The Young's modulus of graphite is taken constant in this work. In literature some studies reported that Young' modulus increases with SOC [70,74]. Nevertheless, few studies exist in literature and a reliable evaluation is missing.

3.1. Concentration and stress computed with non-ideal solution model

The concentration distribution resulting from the insertion and the extraction at low and high C-rates (C/2 and 2C) are reported in Fig. 2.

The concentration is not evenly distributed in the particle, but localized jumps occur during both insertion and extraction, corresponding to the three phase transitions taking place in graphite. This result is consistent with the outcome of Bohn et al. [33], who described phase transitions in graphite with a different thermodynamic approach. Furthermore, the shape of the concentration jumps at the phase boundaries are in agreement also with the work of Song et al. [75], who computed concentration and stress resulting from phase separation in LFP particles with a different modeling approach.

Phase transitions can be detected by the shape of the equilibrium potential: a phase transition is occurring where the potential is flat with respect to x, and the resulting thermodynamic factor drops significantly. Fig. 3 shows that phase transitions occur in the SOC range 0.05–0.12 (transition from phase 1L to 4L), 0.25–0.5 (phase 3L/2L to 2), and 0.5–1 (phase 2 to 1), matching the concentration jump in Fig. 2. The steep concentration gradient is caused by the thermodynamic factor α: it tends to zero where the potential is nearly flat, as shown in Fig. 3, because of the term $\frac{\partial U}{\partial c}$ in Eq. (18). The low thermodynamic factor locally decreases the diffusion coefficient (refer to Eq. (20)), causing the concentration drop observed in Fig. 2.

When a phase transition occurs, the boundary between the two phases moves within the particle. The boundary moves towards the particle center during insertion, and the li-rich phase grows at the expense of the li-poor phase. Vice versa during extraction.

The shift of the phase boundary from the surface to the core is clearly evident during extraction across all phase transitions. During insertion, the moving boundary between phases 1L and 4L, as well as between phases 3L/2L and 2, is visible; however, the boundary between phases 2 and 1 is not discernible. It is likely that a non-Fickian diffusion model would more effectively describe this transition.

From the experimental point of view, Yang et al. [60] measured synchronously the strain and concentration field of graphite electrodes in real-time, and Shi et al. [61] measured just concentration. They observed a concentration trend at electrode scale pretty similar to the one reported in Fig. 2, suggesting that lithium diffusion at particle and electrode scale follows a similar mechanism. Funabiki et al. [62] performed a potential-step chronoamperometry and AC impedance spectroscopy and observed the nucleation and phase-boundary movement of different phases within a graphite electrode, coherent with the phase boundary movement in Fig. 2. At particle scale, Heß et al. [63] applied the thin-layer technique to study graphite particle properties. They suggested a concentration distribution and phase boundary movement in agreement with the results of Fig. 2. In particular, the shape

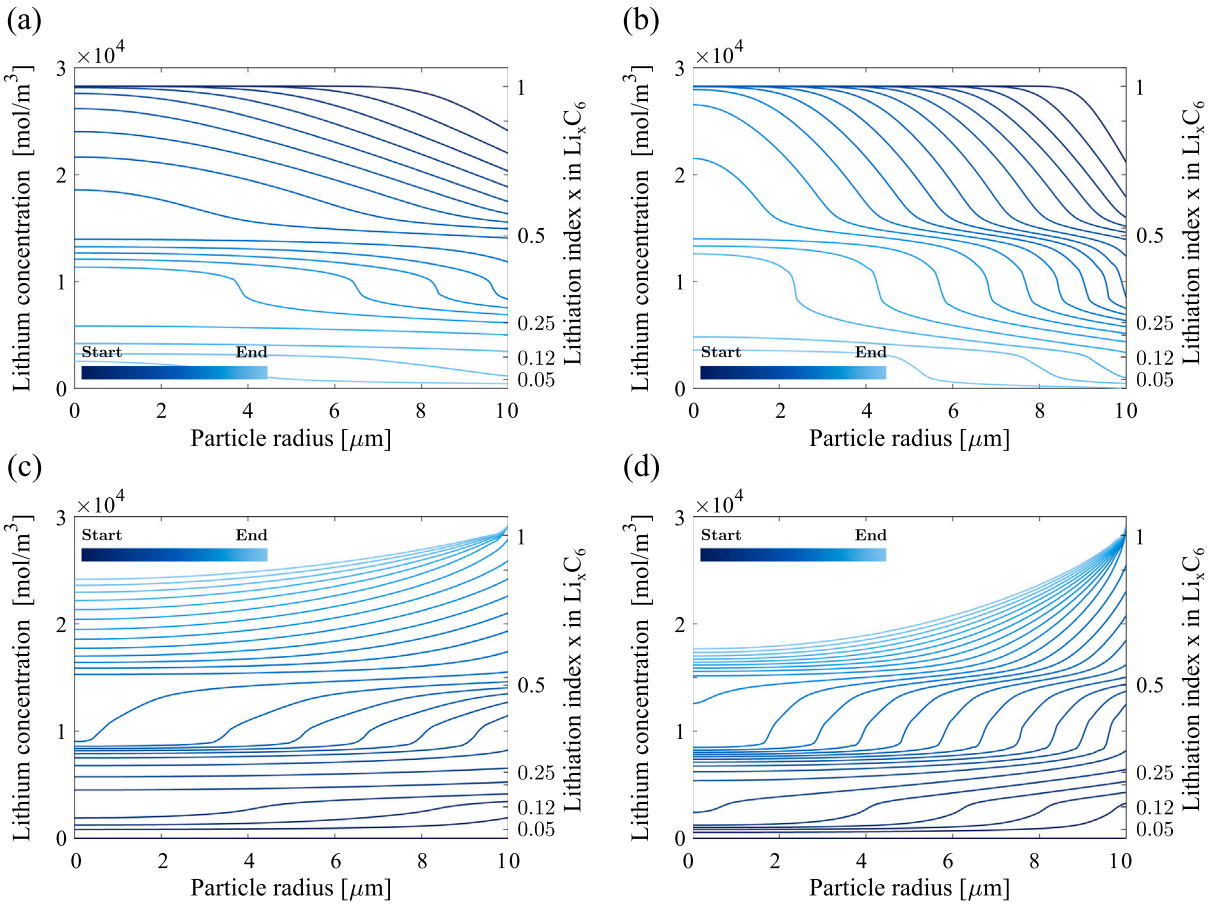

Fig. 2. Concentration of lithium ions within the graphite particle. Blue shades refer to different times: starting from dark blue at the beginning of the operation and gradually fading to light blue towards the end. (a) and (b) refer to extraction at C/2 and 2C, (c) and (d) refer to insertion at C/2 and 2C.

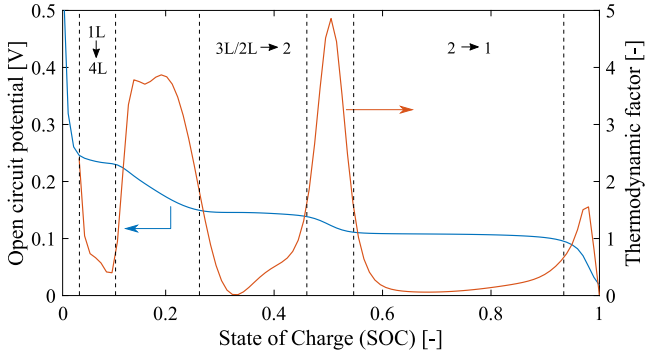

Fig. 3. Open circuit potential (U) and thermodynamic factor (α) of Graphite. The three main phase transitions are depicted in the SOC range where they belong.

of the concentration profile, characterized by jumps between different phases is reported in Figures 10 and 12 in Ref. [63], and the phase boundary movement in Figures 11 and 13 in Ref. [63].

To prove the correctness of the concentration results, it is essential to emphasize that the concentration levels at which phase transitions occurs in Fig. 2 correspond precisely to those observed experimentally. Furthermore, since the stress distribution depends uniquely on the concentration distribution within the active material particle (Eq. (7)), the agreement between the concentration distribution predicted by the model and the experimental observation allows to safely infer that also the stress distribution inside the particle, that cannot be measured experimentally, is correct.

Concerning the effect of the current rate, a higher current causes a steeper concentration gradient because of the greater boundary flux, leading to greater stress.

Radial and hoop stresses within the graphite particle are reported in Fig. 4 for a current rate equal to 1C.

The stresses in the two hoop directions are equal because of the spherical symmetry. Radial stress vanishes at the particle boundary, according to the boundary condition. Furthermore, stress is hydrostatic at the particle center as the stresses in the radial and hoop (principal) directions are equal. Stress sign is exactly the opposite comparing insertion and extraction.

It is worth mentioning that tensile hoop stress is the driving force for cracks propagation, which are likely to grow at the center of the particle during insertion and at the boundary during extraction [12,15,16]. Then, an accurate prediction of hoop stress is needed to evaluate battery degradation in physics based model, considering also fracture mechanics [19,20].

The stresses as a function of the SOC at different current rates are reported in Fig. 5, both in extraction and insertion. The stresses are computed in the most critical position within the particle: radial stress is always computed at the particle center, hoop stress is computed at the particle center during insertion and at the boundary during extraction. Radial and hoop stress at the particle center, reported in Fig. 5, are identical because the stress state is hydrostatic. The current

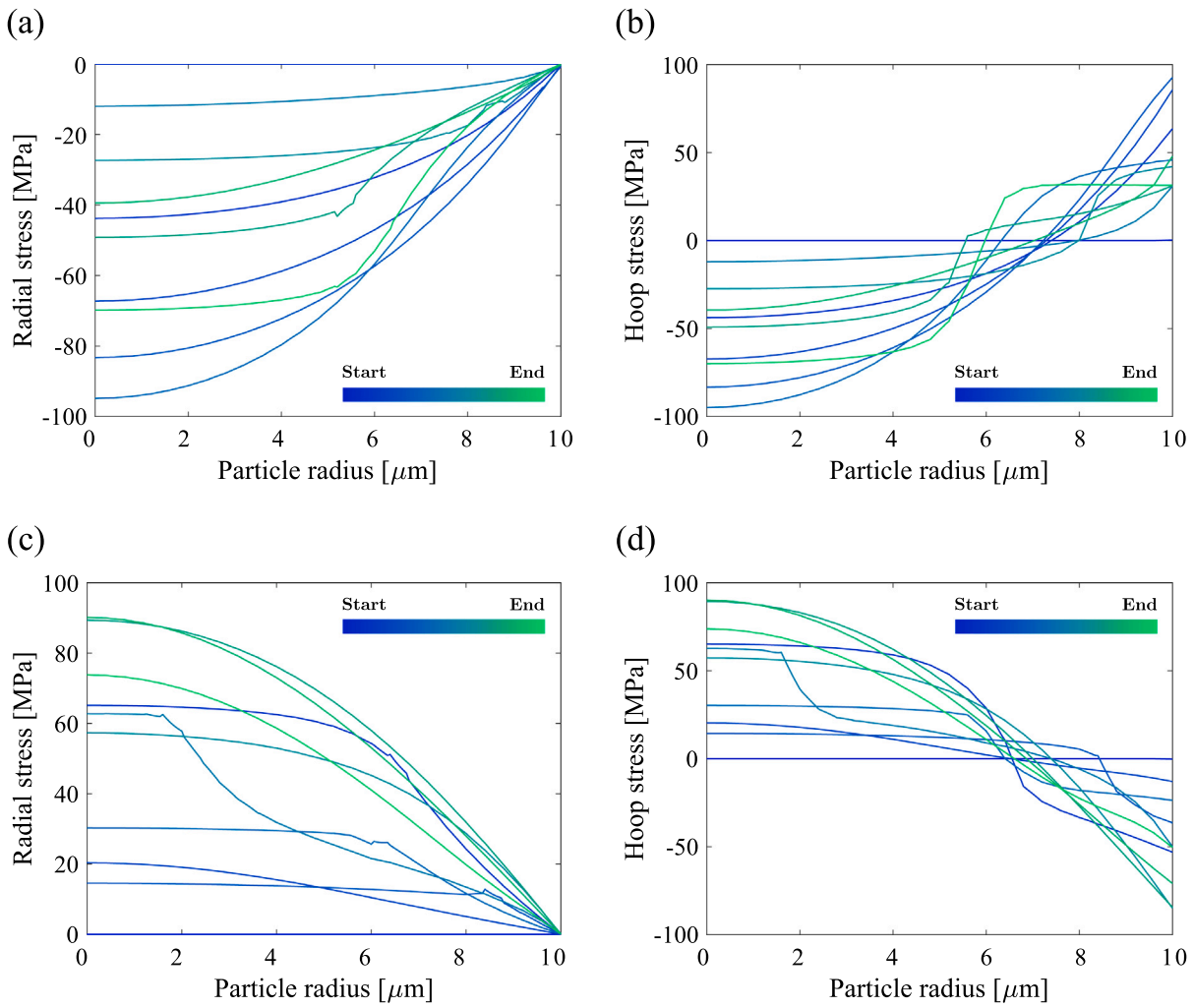

Fig. 4. Stress within the graphite particle. Shades refer to different times: starting from blue at the beginning of the operation and gradually fading to green towards the end. (a) and (b) refer to radial and hoop stress during extraction, and (c) and (d) refer to radial and hoop stress during insertion.

rates are considered up to 3C in extraction (corresponding to the discharge of the full battery) and 2C in insertion (corresponding to the charge of the full battery).

The stress trend is dominated by phase transitions: a stress peak is identifiable at the SOCs where phase transitions occur, namely in the SOC ranges 0.05–0.12, 0.25–0.5, and 0.5–1. The peak is due to the steep concentration gradient at the boundary between the two phases. The stress peaks are wider when longer phase transitions occur (e.g. transition 2–1, which spans half of the SOC window from SOC 0.5 to 1). On the other hand, stress peaks are more localized when the transitions occur in a narrow SOC range (e.g. transition 1L–4L from SOC 0.05 to 0.12).

SOC and DOD are calculated normalizing the capacity with respect to the C/5 capacity, to capture the capacity reduction at higher rates. This ensures that the stress peak remains well-aligned at various current rates. Indeed, stress peaks are caused by phase transitions occurring at the same lithium occupancy (and thus battery capacity), independently on current rate. Some minor misalignments of the stress peaks are observed, probably due to computational errors.

The volumetric strain of the graphite particle, calculated as explained in Eq. (30), is reported in Fig. 6a–b.

$$\varepsilon_v = \frac{\Delta V}{V_0} = \frac{V - V_0}{V_0} = \frac{3uR^2 + 3u^2R + u^3}{R^3} \sim \frac{3u}{R} \tag{30}$$

The volumetric strain of graphite has the characteristic 3-stage shape when the concentration-dependent partial molar volume is considered, according to the data reported in Fig. 1b [51,53]. Then, it is evident that this characteristic is lost as soon as a constant partial molar volume is assumed, as demonstrated by the comparison of solid and dashed lines in Fig. 6a–b. The model results in Fig. 6 fit satisfactorily the volumetric strain measured in lithiated graphite lattice by Schweidler et al. [51].

3.2. Comparison between non-ideal and ideal solution model

In this section, the comparison of the concentration and the stress obtained with the non-ideal solution model proposed in this work and the traditional ideal model, as well as the influence of the concentration-dependent partial molar volume assumption, are discussed.

At first, the comparison between the concentration distribution obtained with the non-ideal and ideal solution model is shown in Fig. 7.

The hypothesis about partial molar volume does not affect the concentration field significantly, keeping similar both with the constant and concentration-dependent assumption. For this reason, a figure justifying this result is not provided. The concentration trend change significantly between non-ideal (Figs. 7a, c) and ideal solution model

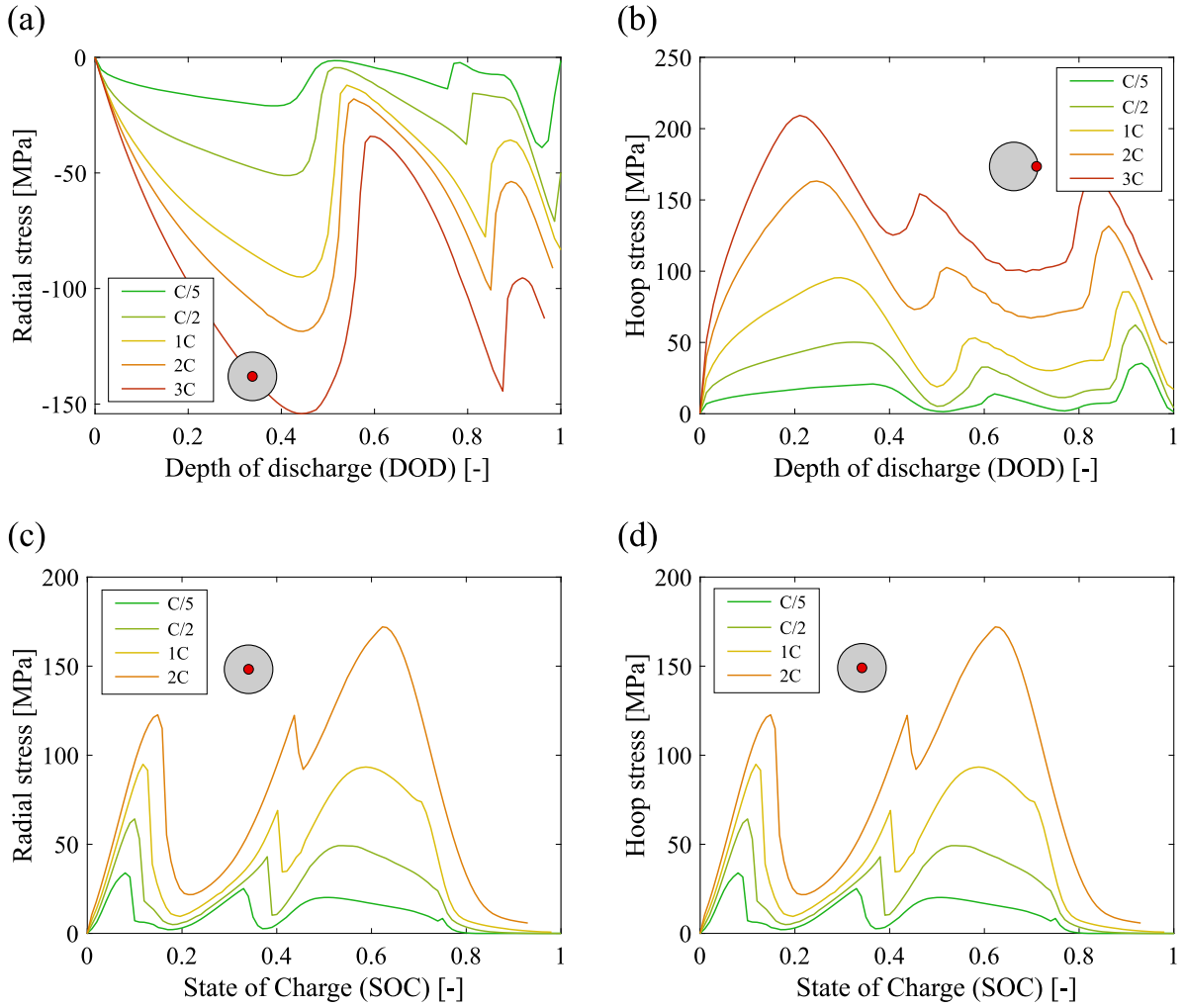

Fig. 5. Stress within the graphite particle as a function of SOC for different current rates. DOD is 1-SOC. SOC and DOD are calculated normalizing the capacity with respect to the C/5 capacity, to capture the capacity reduction at higher rates. The model is the non-ideal solution with concentration-dependent partial molar volume. (a) and (b) refers to radial and hoop stress during extraction, respectively. On the other hand, (c) and (d) refers to radial and hoop stress during insertion, respectively. The red dot in the particle sketch shows the position within the particle where the stress is computed.

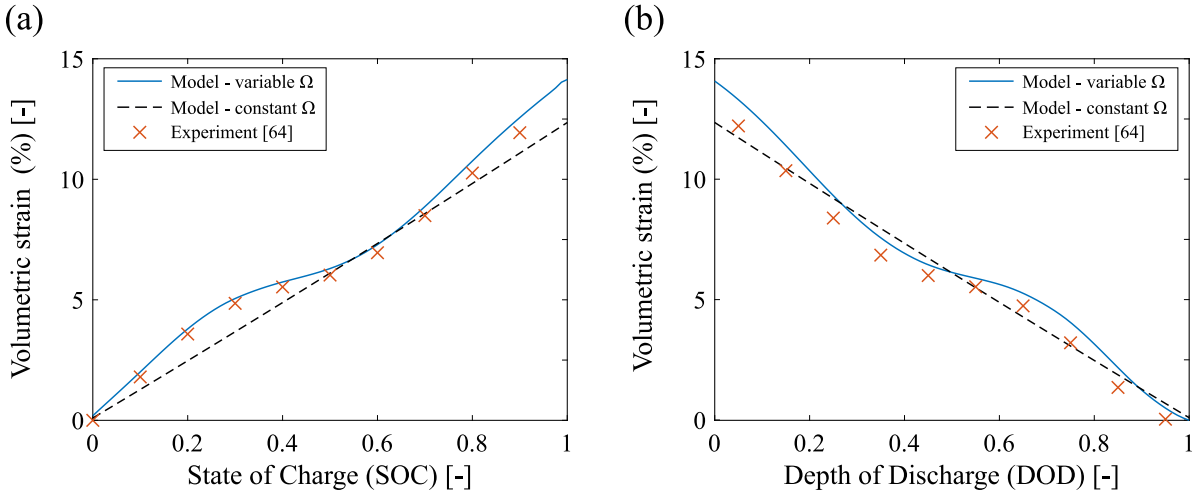

Fig. 6. Volumetric strain of the particle during (a) insertion and (b) extraction at different current rates. Solid and dashed lines refer to the model with concentration-dependent and constant partial molar volume assumptions, respectively. Crosses refer to the experimental measurements [51].

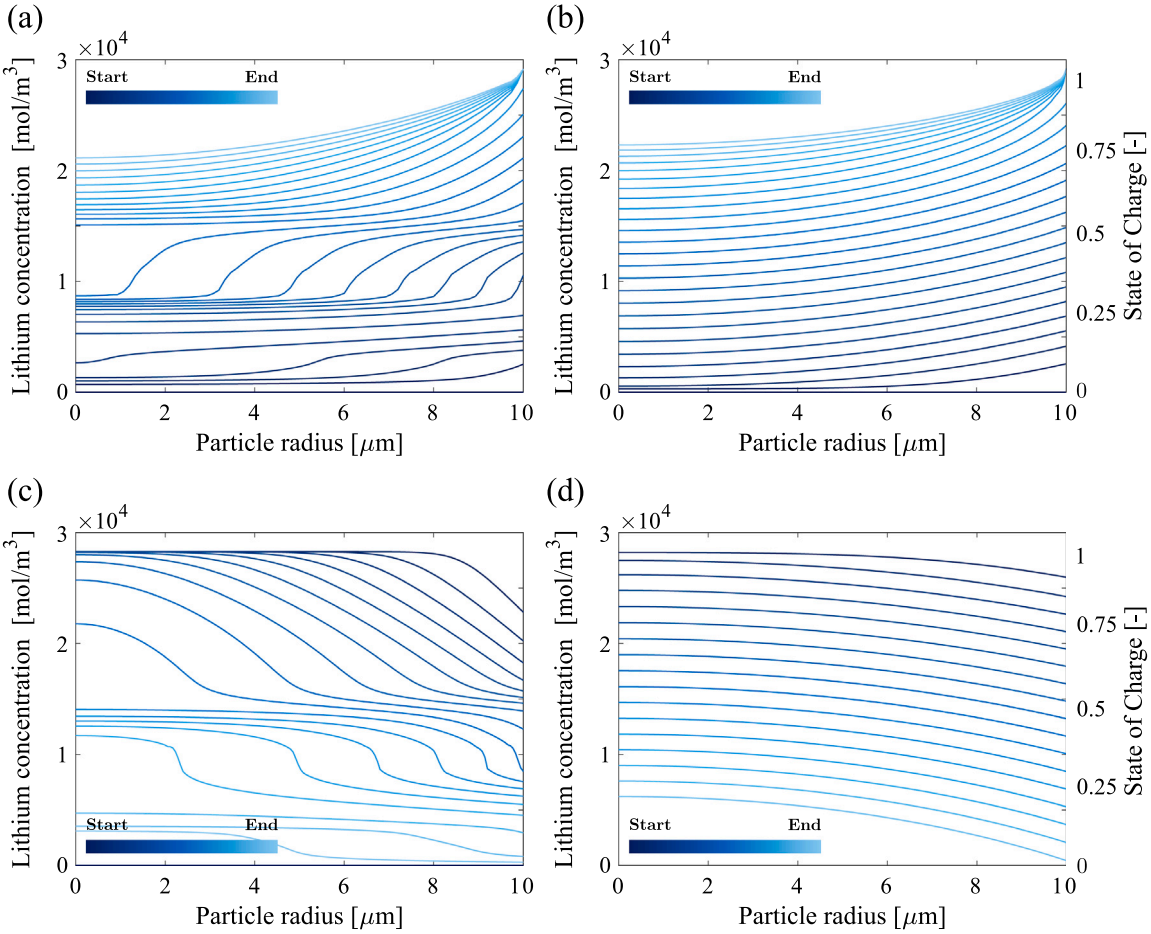

Fig. 7. Comparison among concentration computed with different models: (a) and (c) refer to the non-ideal solution with concentration-dependent partial molar volume, and (b) and (d) refer to the ideal solution with constant partial molar volume. Insertion is reported in (a) and (b), extraction in (c) and (d). Blue shades refer to different times: starting from dark blue at the beginning of the operation and gradually fading to light blue towards the end.

(Figs. 7b, d), as the concentration drops due to phase changes vanish, and a smooth concentration evolution occurs.

With regard to stresses, the same comparison is reported in Fig. 8.

The most significant difference exists between the non-ideal (solid and dashed lines) and ideal solution model (dotted line), with differences up to 85%. The stress trend of the ideal model is flat or linear, on the other hand, the stress trend computed with the non-ideal solution model shows peaks in correspondence of the phase transitions. Indeed, three peaks are observed at SOC 0.1, around SOC 0.4, and from SOC 0.5 to 1, corresponding exactly to the three phase transitions of graphite.

The difference between concentration-dependent and constant assumptions on partial molar volume models is meaningful when considering stress, even if differences are less evident than the ideal/non-ideal comparison. The main change is the reduction (about 40%) of the stress peak due to phase change 3L/2L-2, as it is characterized by a partial molar volume lower than the constant value (refer to Fig. 1a–b). The partial molar volume of the phases 1L/4L is greater than the assumed constant value, reflecting in higher stress (about 30%). On the other hand, constant partial molar volume is similar to the concentration-dependent in the range where the phase transition 1/2 occurs, resulting in similar stress peaks (differences lower than 10%). It is pointed out that these results are obtained for graphite, but they can substantially change for other materials. In the case where partial molar volume shows a greater change, the stress computed with a concentration-dependent partial molar volume becomes substantially different with respect to the constant case.

4. Conclusions

This work assesses the diffusion-induced stress amplification in active materials for electrodes of LIBs showing phase transitions, adopting the non-ideal solution diffusion model. Indeed, the lithium ions concentration inhomogeneity at the phase boundary causes a localized strain mismatch, leading to a severe stress magnification that cannot be captured by the traditional ideal model proposed in the literature. The influence of phase transitions on the lithium diffusion and the consequent stress magnification is considered by defining an equivalent diffusion coefficient, dependent on the equilibrium potential of the host material with respect to Li/Li^+. Furthermore, a concentration-dependent partial molar volume is implemented in the model, in agreement with experimental measurements on phase-change materials.

Graphite is chosen as a case study. The concentration distribution computed with the model is in agreement with the alternating phase transitions observed experimentally with in-situ imaging techniques. The stress is strongly affected by the concentration inhomogeneity due to phase transitions, and it is up to 85% higher with respect to the result of the ideal solution model usually applied in the literature. Stress is influenced by the assumption made on partial molar volume as well, with differences up to 40% with respect to the traditional constant value considered in the literature. In conclusion, this work demonstrates the necessity to include the effects of phase transitions on the diffusion-induced stress calculation, otherwise the stress may

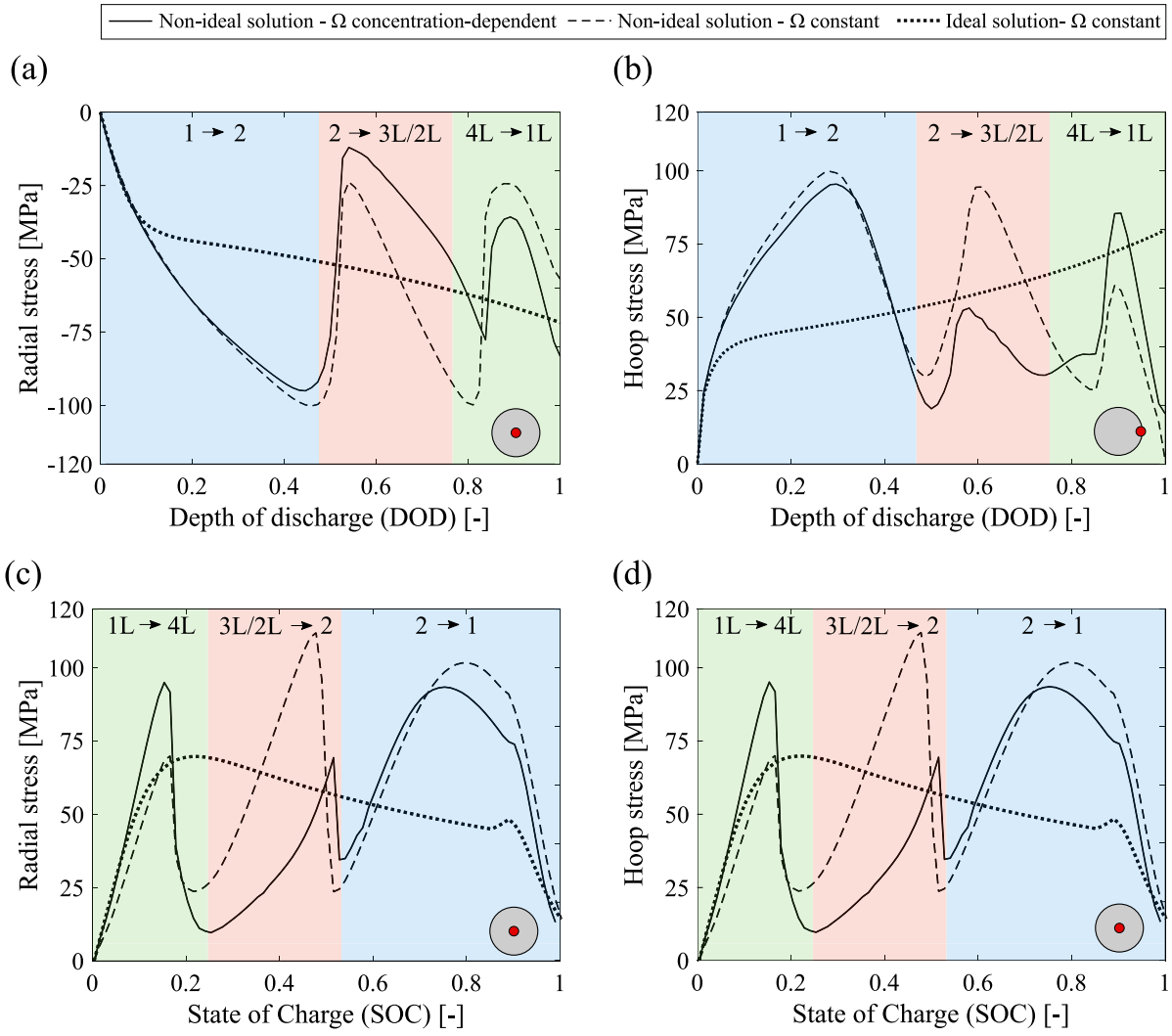

Fig. 8. Comparison among stresses computed with different models: (a) and (b) are Radial and hoop stress in extraction, and (c) and (d) in insertion, respectively. Solid lines refer to the non-ideal solution with concentration-dependent partial molar volume, dashed lines refer to the non-ideal solution with constant partial molar volume, and dotted lines refer to the ideal solution with constant partial molar volume. The red dot in the particle sketch shows the position within the particle where the stress is computed. The SOC ranges where phase transitions occur are displayed with different colors, and the names of the phases are reported at the top of the plots.

be significantly underestimated. This kind of approach is meaningful in the view of evaluating the electrode damage and further elaborate physics-based battery damaging model.

CRediT authorship contribution statement

Davide Clerici: Writing – review & editing, Writing – original draft, Visualization, Validation, Software, Investigation, Formal analysis, Data curation, Conceptualization.

Declaration of competing interest

The authors declare that they have no known competing financial interests or personal relationships that could have appeared to influence the work reported in this paper.

Data availability

No data was used for the research described in the article.

Appendix A. Integration of the mechanical field

The mechanical field is obtained by solving the system of constitutive, congruence, and equilibrium equations reported in Eq. (3). At first, a single equation dependent on displacement is got from the Equation system (3), replacing the congruence Equation ((3)b) in the constitutive equation expressed as Eq. (6), and the latter in the equilibrium Equation ((3)c), resulting in Eq. (A.1).

$$\frac{\partial^2 u}{\partial r^2} + \frac{2}{r}\frac{\partial u}{\partial r} - 2\frac{u}{r^2} = \frac{1}{3}\frac{1+\nu}{1-\nu}\frac{\partial}{\partial r}\left(\int_{c_{sf}}^{c} \Omega\, dc\right) \tag{A.1}$$

Eq. (A.1) is integrated for the first time between zero and a general particle radius, leading to Eq. (A.2). The term $\frac{2}{r}\frac{\partial u}{\partial r}$ is integrated by parts leading to $\frac{2u}{r} + 2\int_0^r \frac{u}{r^2}\, dr$.

$$\frac{\partial u}{\partial r} + \frac{2u}{r} + 2\int_0^r \frac{u}{r^2}\, dr - 2\int_0^r \frac{u}{r^2} = \frac{1}{3}\frac{1+\nu}{1-\nu}\left(\int_{c_{sf}}^{c} \Omega\, dc\right) + K_1 \tag{A.2}$$

where K_1 is the first integration constant.

Eq. (A.2) is multiplied by r^2 and then integrated a second time between zero and a general particle radius, leading to Eq. (A.3). The

term $r^2\frac{\partial u}{\partial r}$ is integrated by parts leading to $ur^2 - 2\int_0^r ru\,dr$.

$$ur^2 + -2\int_0^r ru\,dr + 2\int_0^r ru\,dr = \frac{1}{3}\frac{1+\nu}{1-\nu}\int_0^r\left(\int_{c_{sf}}^{c}\Omega\,dc\right)r^2\,dr + K_1\frac{r^3}{3} + K_2 \tag{A.3}$$

where K_2 is the second integration constant.

Eq. (A.3) is rearranged in Eq. (A.4) to express the radial displacement.

$$u = \frac{1}{3}\frac{1+\nu}{1-\nu}\frac{1}{r^2}\int_0^r\left(\int_{c_{sf}}^{c}\Omega\,dc\right)r^2\,dr + K_1\frac{r}{3} + K_2\frac{1}{r^2} \tag{A.4}$$

The two integration constants are determined by imposing the boundary conditions.

At first, null displacement at the particle center is imposed, resulting immediately in $K_2 = 0$.

The first integration constant (K_1) is got imposing null radial stress at the particle boundary. Then, Eq. (A.4) is derived with respect to r to get $\frac{\partial u}{\partial r}$ in (A.5).

$$\frac{\partial u}{\partial r} = \frac{1}{3}\frac{1+\nu}{1-\nu}\left[\int_{c_{sf}}^{c}\Omega\,dc - \frac{2}{r^3}\int_0^r\left(\int_{c_{sf}}^{c}\Omega\,dc\right)r^2\,dr\right] + \frac{K_1}{3} \tag{A.5}$$

Then, the particle radius (R) is replaced in Eq. (A.4) to get $u(R)$, and in Eq. (A.5) to get $\frac{\partial u}{\partial r}|_{r=R}$, as reported in Eq. (A.6).

$$u(R) = \frac{1}{3}\frac{1+\nu}{1-\nu}\frac{1}{R^2}\int_0^R\left(\int_{c_{sf}}^{c(R)}\Omega\,dc\right)r^2\,dr + K_1\frac{R}{3} \tag{A.6a}$$

$$\left.\frac{\partial u}{\partial r}\right|_{r=R} = \frac{1}{3}\frac{1+\nu}{1-\nu}\left[\int_{c_{sf}}^{c(R)}\Omega\,dc - \frac{2}{R^3}\int_0^R\left(\int_{c_{sf}}^{c(R)}\Omega\,dc\right)r^2\,dr\right] + \frac{K_1}{3} \tag{A.6b}$$

Eq. (A.6) are replaced in the radial stress (Eq. (6)), which is imposed equal to zero, finally obtaining the value of K_1.

The values of the integration constants together with the respective boundary conditions are reported in Eq. (A.7).

$$\begin{cases} u(r=0) = 0 \longrightarrow K_2 = 0 \\ \sigma_r(r=R) = 0 \longrightarrow K_1 = \dfrac{2(1-2\nu)}{1-\nu}\dfrac{1}{R^3}\displaystyle\int_0^R\left(\int_{c_{sf}}^{c(R)}\Omega\,dc\right)r^2\,dr \end{cases} \tag{A.7}$$

The integration constants reported in Eq. (A.7) are replaced in the general displacement solution (Eq. (A.4)) to get the displacement solution reported in Eq. (4).

Appendix B. Model implementation

The model is implemented in Comsol Multiphysics. A 2D axisymmetric semicircle is chosen as the domain to model the spherical particle, and the vertical axis is the symmetry axis. A polar reference system is chosen, where r is the radial coordinate, ϕ is latitude and z is longitude. The model is implemented using the "solid mechanics" and the "transport of diluted species" interfaces. It is preferred to use the latter instead of "the transport of concentrated species" interface because of the greater versatility.

The chemical strain is modeled as "hygroscopic swelling", adding the chemical strain contribution written as Eq. (1) to the elastic strain. Then, the concentration calculated with the "transport of diluted species" interface is attributed to the moisture concentration requested by the "hygroscopic swelling".

The "transport of diluted species" interface is already implemented in Comsol according to the uncoupled model explained in Section 2.2.3. The non-ideal solution model with concentration-dependent partial molar volume explained in Section 2.2.1 is got modifying the flux equations according to Eq. (B.1). The three equations in (B.1) are the flux components along the three polar directions, named in Comsol as "tds.dflux_cr", "tds.dflux_cphi", and "tds.dflux_cz", respectively.

$$\begin{cases} J_r = -D_{rr}(\alpha + k_m c)\frac{\partial c}{\partial r} - D_{rz}(\alpha + k_m c)\frac{\partial c}{\partial z} \\ J_\phi = -D_{\phi r}(\alpha + k_m c)\frac{\partial c}{\partial r} - D\phi z(\alpha + k_m c)\frac{\partial c}{\partial z} \\ J_z = -Dzr(\alpha + k_m c)\frac{\partial c}{\partial r} - Dzz(\alpha + k_m c)\frac{\partial c}{\partial z} \end{cases} \tag{B.1}$$

A non-isotropic diffusion coefficient D can be defined in Comsol, anyway all the components have the same value in this model. Then, the differentials of the flux components are computed in Eq. (B.2).

$$\begin{cases} \dfrac{\partial J_r}{\partial r} = -D_{rr}(\alpha + k_m c)\dfrac{\partial^2 c}{\partial r^2} - D_{rr}\left[\dfrac{\partial \alpha}{\partial c} + \dfrac{\partial k_m}{\partial c}c + k_m\right]\left(\dfrac{\partial c}{\partial r}\right)^2 \\ -D_{rz}(\alpha + k_m c)\dfrac{\partial^2 c}{\partial r \partial z} - D_{rz}\left[\dfrac{\partial \alpha}{\partial c} + \dfrac{\partial k_m}{\partial c}c + k_m\right]\left(\dfrac{\partial c}{\partial z}\dfrac{\partial c}{\partial r}\right) \\ \dfrac{\partial J_{phi}}{\partial \phi} = 0 \\ \dfrac{\partial J_z}{\partial z} = -D_{zr}(\alpha + k_m c)\dfrac{\partial^2 c}{\partial z \partial r} - D_{zr}\left[\dfrac{\partial \alpha}{\partial c} + \dfrac{\partial k_m}{\partial c}c + k_m\right]\left(\dfrac{\partial c}{\partial r}\dfrac{\partial c}{\partial z}\right) \\ -D_{zz}(\alpha + k_m c)\dfrac{\partial^2 c}{\partial z^2} - D_{zz}\left[\dfrac{\partial \alpha}{\partial c} + \dfrac{\partial k_m}{\partial c}c + k_m\right]\left(\dfrac{\partial c}{\partial z}\right)^2 \end{cases} \tag{B.2}$$

Finally, the residual equation (named "tds.Res_c" in Comsol) is modified as follows in Eq. (B.3), with the results of Eq. (B.2).

$$\nabla \cdot J = R; \quad \frac{\partial J_r}{\partial r} + \frac{\partial J_\phi}{\partial \phi} + \frac{\partial J_z}{\partial z} = R \tag{B.3}$$

Table C.3
Graphite properties.

Partial molar volume	$-2.50\,10^{-3}(soc)^7 + 9.70\,10^{-3}(soc)^6 - 1.46\,10^{-2}(soc)^5$
Lithiation	$+1.05\,10^{-2}(soc)^4 - 3.62\,10^{-3}(soc)^3 + 5.14\,10^{-4}(soc)^2$ $-2.70\,10^{-5}(soc) + 6.66\,10^{-6}$
Partial molar volume	$-2.53\,10^{-3}(soc)^7 + 9.91\,10^{-3}(soc)^6 - 1.49\,10^{-2}(soc)^5$ $+1.06\,10^{-2}(soc)^4 - 3.41\,10^{-3}(soc)^3 + 3.13\,10^{-4}(soc)^2$
Delithiation	$+2.84\,10^{-5}(soc) + 2.71\,10^{-6}$
Open circuit voltage	$0.124 + 1.5\,exp(-150\,soc) + 0.0155\,tanh(\frac{soc-0.105}{0.029})$ $-0.011\,tanh(\frac{soc-0.124}{0.0226}) - 0.102\,tanh(\frac{soc-0.194}{0.142})$ $+0.0347\,tanh(\frac{soc-0.286}{0.083}) - 0.0147\,tanh(\frac{soc-0.5}{0.034})$ $-0.0045\,tanh(\frac{soc-0.9}{0.119}) - 0.022\,tanh(\frac{soc-0.98}{0.0164})$ $-0.035\,tanh(\frac{soc-0.99}{0.05})$

Appendix C. Interpolated quantities

The interpolated Equilibrium potential of graphite vs Li/Li^+ taken from Christensen et al. [24] and the interpolation of partial molar volume computed with Eq. (2) from the volumetric strain measurements on lattice structure of graphite [51] are reported in Table C.3.

References

[1] Clerici D, et al. Mechanics of lithium-ion batteries-a modelling and experimental perspective. Politecnico di Torino; 2024.

[2] Clerici D, Pistorio F, Mocera F, Somà A. Mechanical characterization and modelling of lithium-ion batteries. Transp Res Procedia 2023;70:276–83.

[3] Clerici D, Martelli S, Mocera F, Somà A. Mechanical characterization of lithium-ion batteries with different chemistries and formats. J Energy Storage 2024;84:110899.

[4] Clerici D, Mocera F, Somà A. Experimental characterization of lithium-ion cell strain using laser sensors. Energies 2021;14(19):6281.
[5] Verbrugge MW, Cheng Y-T. Stress and strain-energy distributions within diffusion-controlled insertion-electrode particles subjected to periodic potential excitations. J Electrochem Soc 2009;156(11):A927.
[6] Iqbal N, Lee S. Anisotropic model to describe chemo-mechanical response of Ni-rich cathode materials. Int J Mech Sci 2024;269:109034.
[7] Wang B, Aifantis KE. Probing the effect of surface parameters and particle size in the diffusion-induced stress of electrodes during lithium insertion. Int J Mech Sci 2022;215:106917.
[8] Hofmann T, Westhoff D, Feinauer J, Andrä H, Zausch J, Schmidt V, et al. Electro-chemo-mechanical simulation for lithium ion batteries across the scales. Int J Solids Struct 2020;184:24–39.
[9] Zhao Y, Stein P, Bai Y, Al-Siraj M, Yang Y, Xu B-X. A review on modeling of electro-chemo-mechanics in lithium-ion batteries. J Power Sources 2019;413:259–83.
[10] Pistorio F, Clerici D, Mocera F, Somà A. Coupled electrochemical–mechanical model for fracture analysis in active materials of lithium ion batteries. J Power Sources 2023;580:233378.
[11] Clerici D, Pistorio F, Somà A. Design and fracture mechanics of lithium-ion batteries. Procedia Struct Integr 2024;58:23–9.
[12] Clerici D, Mocera F, Pistorio F. Analysis of fracture behaviour in active materials for lithium ion batteries. In: IOP conference series: materials science and engineering, vol. 1214, (no. 1):IOP Publishing; 2022, 012018.
[13] Pistorio F, Clerici D, Somà A. Analytical computation of stress intensity factor for active material particles of lithium ion batteries. Eng Fract Mech 2023;292:109597.
[14] Pistorio F, Clerici D. Analytical computation of stress intensity factor for multi-physics problems. In: IOP conference series: materials science and engineering, vol. 1306, (no. 1):IOP Publishing; 2024, 012009.
[15] Pistorio F, Clerici D, Mocera F, Somà A. Review on the experimental characterization of fracture in active material for lithium-ion batteries. Energies 2022;15(23):9168.
[16] Pistorio F, Clerici D, Mocera F, Somà A. Review on the numerical modeling of fracture in active materials for lithium ion batteries. J Power Sources 2023;566:232875.
[17] Birkl CR, Roberts MR, McTurk E, Bruce PG, Howey DA. Degradation diagnostics for lithium ion cells. J Power Sources 2017;341:373–86.
[18] Iqbal N, Ali Y, Lee S. Mechanical degradation analysis of a single electrode particle with multiple binder connections: a comparative study. Int J Mech Sci 2020;188:105943.
[19] O'Kane SE, Ai W, Madabattula G, Alonso-Alvarez D, Timms R, Sulzer V, et al. Lithium-ion battery degradation: how to model it. Phys Chem Chem Phys 2022;24(13):7909–22.
[20] Dong G, Wei J. A physics-based aging model for lithium-ion battery with coupled chemical/mechanical degradation mechanisms. Electrochim Acta 2021;395:139133.
[21] Mocera F, Somà A, Clerici D. Study of aging mechanisms in lithium-ion batteries for working vehicle applications. In: 2020 fifteenth international conference on ecological vehicles and renewable energies. IEEE; 2020, p. 1–8.
[22] Zhang X, Shyy W, Sastry AM. Numerical simulation of intercalation-induced stress in li-ion battery electrode particles. J Electrochem Soc 2007;154(10):A910.
[23] Zhang X, Sastry AM, Shyy W. Intercalation-induced stress and heat generation within single lithium-ion battery cathode particles. J Electrochem Soc 2008;155(7):A542.
[24] Christensen J, Newman J. Stress generation and fracture in lithium insertion materials. J Solid State Electrochem 2006;10:293–319.
[25] Newman J, Balsara NP. Electrochemical systems. John Wiley & Sons; 2021.
[26] Clerici D, Mocera F, Somà A. Analytical solution for coupled diffusion induced stress model for lithium-ion battery. Energies 2020;13(7):1717.
[27] Li Y, Zhang K, Zheng B, Yang F. Effect of local deformation on the coupling between diffusion and stress in lithium-ion battery. Int J Solids Struct 2016;87:81–9.
[28] Clerici D, Mocera F. Micro-scale modeling of lithium-ion battery. In: IOP conference series: materials science and engineering, vol. 1038, (no. 1):IOP Publishing; 2021, 012007.
[29] Clerici D, Mocera F, Somà A. Shape influence of active material micro-structure on diffusion and contact stress in lithium-ion batteries. Energies 2020;14(1):134.
[30] Van der Ven A, Bhattacharya J, Belak AA. Understanding li diffusion in Li-intercalation compounds. Acc Chem Res 2013;46(5):1216–25.
[31] Zhou H, et al. Two-phase transition of Li-intercalation compounds in Li-ion batteries. Mater Today 2014;17(9):451–63.
[32] Baker DR, Verbrugge MW. Intercalate diffusion in multiphase electrode materials and application to lithiated graphite. J Electrochem Soc 2012;159(8):A1341.
[33] Bohn E, Eckl T, Kamlah M, McMeeking R. A model for lithium diffusion and stress generation in an intercalation storage particle with phase change. J Electrochem Soc 2013;160(10):A1638.
[34] Bucci G, Swamy T, Bishop S, Sheldon BW, Chiang Y-M, Carter WC. The effect of stress on battery-electrode capacity. J Electrochem Soc 2017;164(4):A645.
[35] Wu B, Lu W. A consistently coupled multiscale mechanical–electrochemical battery model with particle interaction and its validation. J Mech Phys Solids 2019;125:89–111.
[36] Baker DR, Verbrugge MW. Multi-species, multi-reaction model for porous intercalation electrodes: Part I. Model formulation and a perturbation solution for low-scan-rate, linear-sweep voltammetry of a spinel lithium manganese oxide electrode. J Electrochem Soc 2018;165(16):A3952.
[37] Baker DR, Verbrugge MW, Gu W. Multi-species, multi-reaction model for porous intercalation electrodes: Part II. Model-experiment comparisons for linear-sweep voltammetry of spinel lithium manganese oxide electrodes. J Electrochem Soc 2019;166(4):A521.
[38] Tavassol H, Jones EM, Sottos NR, Gewirth AA. Electrochemical stiffness in lithium-ion batteries. Nat Mater 2016;15(11):1182–7.
[39] Cahn JW. Free energy of a nonuniform system. II. Thermodynamic basis. J Chem Phys 1959;30(5):1121–4.
[40] Han B, Van der Ven A, Morgan D, Ceder G. Electrochemical modeling of intercalation processes with phase field models. Electrochim Acta 2004;49(26):4691–9.
[41] Hofmann T, Müller R, Andrä H, Zausch J. Numerical simulation of phase separation in cathode materials of lithium ion batteries. Int J Solids Struct 2016;100:456–69.
[42] Singh GK, Ceder G, Bazant MZ. Intercalation dynamics in rechargeable battery materials: General theory and phase-transformation waves in LiFePO4. Electrochim Acta 2008;53(26):7599–613.
[43] Bai P, Cogswell DA, Bazant MZ. Suppression of phase separation in LiFePO4 nanoparticles during battery discharge. Nano Lett 2011;11(11):4890–6.
[44] Zhang Q, White RE. Moving boundary model for the discharge of a LiCoO2 electrode. J Electrochem Soc 2007;154(6):A587.
[45] Srinivasan V, Newman J. Discharge model for the lithium iron-phosphate electrode. J Electrochem Soc 2004;151(10):A1517.
[46] Khandelwal A, Hariharan KS, Kumar VS, Gambhire P, Kolake SM, Oh D, et al. Generalized moving boundary model for charge–discharge of LiFePO4/C cells. J Power Sources 2014;248:101–14.
[47] Khandelwal A, Hariharan KS, Gambhire P, Kolake SM, Yeo T, Doo S. Thermally coupled moving boundary model for charge–discharge of LiFePO4/C cells. J Power Sources 2015;279:180–96.
[48] Shin H-C, Pyun S-I. The kinetics of lithium transport through Li1- δCoO2 by theoretical analysis of current transient. Electrochim Acta 1999;45(3):489–501.
[49] Wu H, Xie Z, Wang Y, Lu C, Ma Z. Modeling diffusion–induced stress on two-phase lithiation in lithium-ion batteries. Eur J Mech A Solids 2018;71:320–5.
[50] Deshpande R, Cheng Y-T, Verbrugge MW, Timmons A. Diffusion induced stresses and strain energy in a phase-transforming spherical electrode particle. J Electrochem Soc 2011;158(6):A718.
[51] Schweidler S, de Biasi L, Schiele A, Hartmann P, Brezesinski T, Janek J. Volume changes of graphite anodes revisited: a combined operando X-ray diffraction and in situ pressure analysis study. J Phys Chem C 2018;122(16):8829–35.
[52] Winter M, Besenhard JO, Spahr ME, Novak P. Insertion electrode materials for rechargeable lithium batteries. Adv Mater 1998;10(10):725–63.
[53] Didier C, Pang WK, Guo Z, Schmid S, Peterson VK. Phase evolution and intermittent disorder in electrochemically lithiated graphite determined using in operando neutron diffraction. Chem Mater 2020;32(6):2518–31.
[54] Koerver R, Zhang W, de Biasi L, Schweidler S, Kondrakov AO, Kolling S, et al. Chemo-mechanical expansion of lithium electrode materials–on the route to mechanically optimized all-solid-state batteries. Energy Environ Sci 2018;11(8):2142–58.
[55] de Biasi L, Kondrakov AO, Geßwein H, Brezesinski T, Hartmann P, Janek J. Between scylla and charybdis: balancing among structural stability and energy density of layered NCM cathode materials for advanced lithium-ion batteries. J Phys Chem C 2017;121(47):26163–71.
[56] Dolotko O, Senyshyn A, Mühlbauer M, Nikolowski K, Ehrenberg H. Understanding structural changes in NMC Li-ion cells by in situ neutron diffraction. J Power Sources 2014;255:197–203.
[57] Clerici D, Mocera F, Soma A. Electrochemical–mechanical multi-scale model and validation with thickness change measurements in prismatic lithium-ion batteries. J Power Sources 2022;542:231735.
[58] Rieger B, Schlueter S, Erhard SV, Jossen A. Strain propagation in lithium-ion batteries from the crystal structure to the electrode level. J Electrochem Soc 2016;163(8):A1595.
[59] Pegel H, von Kessel O, Heugel P, Deich T, Tübke J, Birke KP, et al. Volume and thickness change of NMC811| SiOx-graphite large-format lithium-ion cells: from pouch cell to active material level. J Power Sources 2022;537:231443.
[60] Yang W, Xie H, Shi B, Song H, Qiu W, Zhang Q. In-situ experimental measurements of lithium concentration distribution and strain field of graphite electrodes during electrochemical process. J Power Sources 2019;423:174–82.
[61] Shi B, Kang Y, Xie H, Song H, Zhang Q. In situ measurement and experimental analysis of lithium mass transport in graphite electrodes. Electrochim Acta 2018;284:142–8.
[62] Funabiki A, Inaba M, Abe T, Ogumi Z. Nucleation and phase-boundary movement upon stage transformation in lithium–graphite intercalation compounds. Electrochim Acta 1999;45(6):865–71.

[63] Heß M, Novák P. Shrinking annuli mechanism and stage-dependent rate capability of thin-layer graphite electrodes for lithium-ion batteries. Electrochim Acta 2013;106:149–58.
[64] Mukhopadhyay A, Sheldon BW. Deformation and stress in electrode materials for Li-ion batteries. Prog Mater Sci 2014;63:58–116.
[65] Prussin S. Generation and distribution of dislocations by solute diffusion. J Appl Phys 1961;32(10):1876–81.
[66] Less GB, Seo JH, Han S, Sastry AM, Zausch J, Latz A, et al. Micro-scale modeling of Li-ion batteries: parameterization and validation. J Electrochem Soc 2012;159(6):A697.
[67] Farkhondeh M, Delacourt C. Mathematical modeling of commercial LiFePO4 electrodes based on variable solid-state diffusivity. J Electrochem Soc 2011;159(2):A177.
[68] Mastali M, Farkhondeh M, Farhad S, Fraser RA, Fowler M. Electrochemical modeling of commercial LiFePO4 and graphite electrodes: kinetic and transport properties and their temperature dependence. J Electrochem Soc 2016;163(13):A2803.
[69] Sethuraman VA, Van Winkle N, Abraham DP, Bower AF, Guduru PR. Real-time stress measurements in lithium-ion battery negative-electrodes. J Power Sources 2012;206:334–42.
[70] Li D, Wang Y. In-situ measurements of mechanical property and stress evolution of commercial graphite electrode. Mater Des 2020;194:108887.
[71] Gottschalk L, Müller J, Schoo A, Baasch E, Kwade A. Spherical graphite anodes: Influence of particle size distribution and multilayer structuring in lithium-ion battery cells. Batteries 2024;10(2):40.
[72] Guo H-j, Li X-h, Zhang X-m, Wang H-q, Wang Z-x, Peng W-j. Diffusion coefficient of lithium in artificial graphite, mesocarbon microbeads, and disordered carbon. New Carbon Mater 2007;22(1):7–10.
[73] Wang A, O'Kane S, Planella FB, Le Houx J, O'Regan K, Zyskin M, et al. Review of parameterisation and a novel database (LiionDB) for continuum li-ion battery models. Prog Energy 2022;4(3):032004.
[74] Qi Y, Guo H, Hector LG, Timmons A. Threefold increase in the Young's modulus of graphite negative electrode during lithium intercalation. J Electrochem Soc 2010;157(5):A558.
[75] Song Y, Li Z, Soh A, Zhang J. Diffusion of lithium ions and diffusion-induced stresses in a phase separating electrode under galvanostatic and potentiostatic operations: Phase field simulations. Mech Mater 2015;91:363–71.